BNL-230367-2026-TECH

Loss Factor of Axisymmetric and Rectangular Tapered Collimators from Optical to Inductive Regimes

M. Rahman

October 2026

Electron-Ion Collider Project

Brookhaven National Laboratory

U.S. Department of Energy

USDOE Office of Science (SC), Nuclear Physics (NP)

Notice: This technical note has been authored by employees of Brookhaven Science Associates, LLC under Contract No. with the U.S. Department of Energy. The publisher by accepting the technical note for publication acknowledges that the United States Government retains a non-exclusive, paid-up, irrevocable, world-wide license to publish or reproduce the published form of this technical note, or allow others to do so, for United States Government purposes.

DISCLAIMER

This report was prepared as an account of work sponsored by an agency of the United States Government. Neither the United States Government nor any agency thereof, nor any of their employees, nor any of their contractors, subcontractors, or their employees, makes any warranty, express or implied, or assumes any legal liability or responsibility for the accuracy, completeness, or any third party's use or the results of such use of any information, apparatus, product, or process disclosed, or represents that its use would not infringe privately owned rights. Reference herein to any specific commercial product, process, or service by trade name, trademark, manufacturer, or otherwise, does not necessarily constitute or imply its endorsement, recommendation, or favoring by the United States Government or any agency thereof or its contractors or subcontractors. The views and opinions of authors expressed herein do not necessarily state or reflect those of the United States Government or any agency thereof.

Loss Factor of Axisymmetric and Rectangular Tapered Collimators from Optical to Inductive Regimes

Md Wahidur Rahman,* Alexei Blednykh, Gang Wang, and Xiaofeng Gu
Brookhaven National Laboratory, Electron-Ion Collider, Upton, New York 11973-5000, USA

In this work, we investigate the loss factor of axisymmetric and rectangular tapered collimators over a broad range of bunch lengths and geometrical parameters using the electromagnetic simulation codes ECHO and GdfidL. The calculations are performed for Gaussian bunches of rms length σ_s, with the collimator geometry characterized by the minimum and maximum apertures b and d, taper length L, and chamber width W for rectangular structures. For short bunches and tapered collimators with $d-b>b$, we extend the phenomenological formula previously obtained for axisymmetric to rectangular tapered collimators, describing the dependence of the loss factor on bunch length and taper geometry through an arctangent function of the scaling parameter $\mu d^2/(\sigma_s L)$. We demonstrate that this parameter is related to a Fresnel number and, by combining diffraction theory with the electrodynamics of the beam-induced image charge, analytically explain the factor of two between the coefficients $\mu=0.2$ and $\mu=0.4$ for axisymmetric and rectangular collimators, respectively. The resulting expression is applicable to rectangular collimators with $W/(2d)\geq 1.8$, extending its validity beyond the idealized flat geometry. For longer bunches, we identify the transition from the optical to the inductive regime and derive an analytical expression for the loss factor based on the cutoff wavenumber of the lowest relevant electromagnetic mode.

I. INTRODUCTION

The vacuum system of an accelerator contains numerous components with changes in cross section. Collimators are among the most critical of these components, as they intercept the beam halo, localize particle losses, and protect sensitive equipment and detectors. In a collider complex such as the Electron-Ion Collider (EIC), collimators in the Electron Storage Ring (ESR) protect the interaction region and reduce detector backgrounds [1]. To avoid abrupt changes in cross section at the narrow aperture and to reduce the beam coupling impedance, the collimator jaws are tapered over a length L from the chamber half-aperture d to the minimum half-aperture b (see Fig. 1). A charged-particle bunch passing through such a transition excites electromagnetic wakefields that can lead to energy loss and beam quality degradation [2–6]. The strength of these wakefields, which must be minimized, depends on the bunch length, transition regime, and collimator geometry, including the aperture dimensions, taper length, and cross-sectional shape [7, 8].

The longitudinal impedance of tapered collimators is known analytically in two limits. At low frequencies it is inductive, as derived by Yokoya for round tapers [9] and by Stupakov for arbitrary cross sections [10]. At high frequencies, the optical approximation gives a real impedance determined by the transverse geometry alone [5, 11]. The conventional optical approximation is valid when the transition length is short compared with the catch-up distance at high frequency [11]. Between these limits, Stupakov, Bane and Zagorodnov [5] formulated the problem with a parabolic (paraxial) equation, and Podobedov and Stupakov [12] computed the impedance of round collimators with an eigenmode method. Based on ECHO [13, 14] and GdfidL [15] simulations, Blednykh and Krinsky [2, 3] found that the loss factor of short bunches follows a phenomenological arctan law in $d^2/(\sigma_s L)$, with coefficients $\mu_{\rm rnd}=0.2$ and $\mu_{\rm flt}=0.4$ for round and flat collimators, respectively.

For a Gaussian bunch with rms length σ_s, the loss factor is defined as

$$k_{\parallel}(\sigma_s)=\frac{\Delta E}{Q^2}=\int_{-\infty}^{\infty} W_{\parallel}(s)\,\lambda(s)\,ds, \tag{1}$$

where ΔE is the energy lost by the bunch, Q is the total charge, $\lambda(s)$ is the normalized longitudinal charge distribution, and $W_{\parallel}(s)$ is the longitudinal wake potential.

The tapered axisymmetric and rectangular collimator are shown in Fig. 1(a), and in Fig. 1(b), respectively. In the axisymmetric collimator, b and d denote the smaller and larger radii, respectively. In the rectangular collimator, b and d denote the smaller and larger vertical half-apertures, while W denotes the full chamber width. In both geometries, L is the taper length and g is the length of the narrow central section.

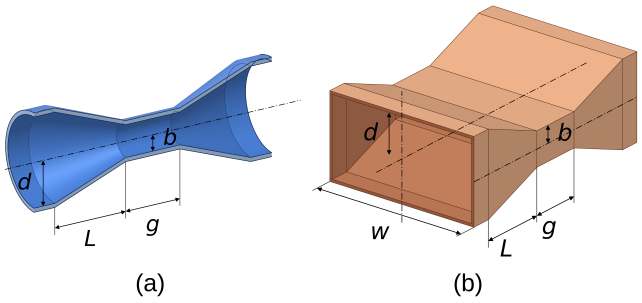


FIG. 1. (a) Tapered axisymmetric collimator. (b) Tapered rectangular collimator.

* Corresponding author: mrahman5@bnl.gov

In this paper, the loss factor of round and flat tapered collimators is computed with GdfidL and ECHO and described by a single formula, Eq. (2), that covers the optical and inductive regimes. The resulting two-regime loss factor model is given by

$$k_{\parallel,\mathrm{tpr}}(\sigma_s) = \begin{cases} k_{\parallel,\mathrm{step}}(\sigma_s)\left[\dfrac{2}{\pi}\tan^{-1}\left(\dfrac{\mu d^2}{\sigma_s L}\right)\right]^2, & \sigma_s \le \sigma_i \\ \text{(optical)} \\ k_{\parallel,\mathrm{step}}(\sigma_i)\left[\dfrac{2}{\pi}\tan^{-1}\left(\dfrac{\mu d^2}{\sigma_i L}\right)\right]^2 & \sigma_s > \sigma_i \\ \times\left(\dfrac{\sigma_i}{\sigma_s}\right)^2 \exp\left[-k_c^2\left(\sigma_s^2-\sigma_i^2\right)\right], & \text{(inductive)} \end{cases} \tag{2}$$

where $k_{\parallel,\mathrm{step}}$ is the loss factor of step collimator, $\sigma_i = 1/(\sqrt{2\ln 2}\,k_c)$ defines the optical to inductive regime transition bunch length, and k_c is the cutoff wavenumber of the lowest relevant electromagnetic mode of the collimator, with $k_c^{\mathrm{rnd}} = j_{01}/d$ for the round and $k_c^{\mathrm{flat}} = \pi\sqrt{1/W^2 + 1/(2d)^2}$ for the flat geometry, respectively. Here, j_{01} is the first zero of the Bessel function of the first kind, J_0. Thus, the cutoff wavenumber, k_c depends primarily on d for the round collimator, and on both d and chamber width W for the flat collimator.

The factor of two between these two collimators, $\mu_{\mathrm{flt}}/\mu_{\mathrm{rnd}} \approx 2$ discussed in Ref [3], is derived here analytically from a Fresnel number [16–18] defined by the transverse extent of the image charge, with $N_F^{\mathrm{rnd}} = d^2/(2\sigma_s L)$ and $N_F^{\mathrm{flt}} = d^2/(\sigma_s L)$. In this interpretation, the bunch length provides the characteristic longitudinal scale, the taper length represents the propagation distance, and the transverse extent of the image charge distribution defines the effective aperture. The taper arguments can be written as $\mu_{\mathrm{rnd}} d^2/(\sigma_s L) = 0.4 N_F^{\mathrm{rnd}}$ and $\mu_{\mathrm{flt}} d^2/(\sigma_s L) = 0.4 N_F^{\mathrm{flt}}$. Thus,

$$\frac{\mu_{\mathrm{flt}}}{\mu_{\mathrm{rnd}}} = \frac{N_F^{\mathrm{flt}}}{N_F^{\mathrm{rnd}}} \approx 2, \tag{3}$$

showing the empirical relation [3] is consistent with the corresponding Fresnel number ratio. As the bunch length increases, the system departs from the high frequency optical limit and diffraction effects become more important [5].

We compare the normalized loss factor for the round and flat tapered collimators using the Fresnel number scaling $\sigma_s L/(\mu d^2)$ shown in Fig. 2. For $N_F \gg 1$, both geometries approach the abrupt-step limit. As N_F decreases ($N_F \lesssim 1$), the loss factors follow a similar tapered optical scaling. For sufficiently long bunches ($\sigma_s > \sigma_i$), the behavior transitions to the inductive regime, where the curves separate according to the geometry-dependent transition bunch lengths σ_i^{rnd} and σ_i^{flt}.

In this work, we extend the loss factor analysis to a broad range of bunch lengths for both axisymmetric and rectangular tapered collimators. First, we investigate the dependence of the loss factor on bunch length and geometric parameters and describe the transition from the optical to the inductive regime. We then examine the relation between the conventional catch-up distance criterion and the short-bunch behavior. Next, we develop a two-regime loss factor model valid from short to long bunches and compare it with numerical results from ECHO and GdfidL. Finally, we apply the model to estimate beam-induced power loss in an Electron Storage Ring (ESR) collimator of the Electron-Ion Collider (EIC).

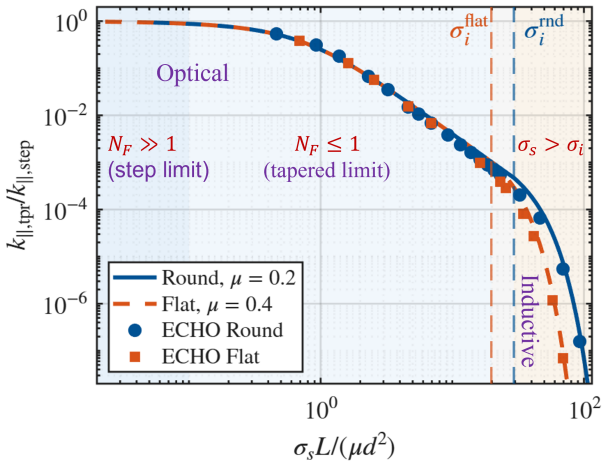


FIG. 2. Normalized loss factor for round and flat tapered collimators obtained from the loss factor model (Eq. (2)) and numerical simulations on the scaled Fresnel axis. The reference geometry is $b = 4.6$ mm, $d = 18$ mm, $L = 300$ mm, and $W = 67$ mm. The vertical dashed lines indicate the optical and inductive transition $\sigma_i^{\mathrm{rnd}} = 6.34$ mm and $\sigma_i^{\mathrm{flt}} = 8.55$ mm. The inductive regime starts at $\sigma_s = \sigma_i$, where $N_F = N_F(\sigma_i) \propto d/L$ given by Eqs. (15) and (16). The shaded regions indicate the optical (light blue) regime, including the step and tapered limits, and the inductive (light brown) regime.

II. FRESNEL NUMBER OF A TAPERED COLLIMATORS

The phenomenological arctangent taper factor in Eq. (2) is derived analytically in this work through Fresnel-number analysis. In diffraction theory, the Fresnel number $N_F^{\mathrm{opt}} = a^2/(\lambda L)$ compares a transverse aperture a with the diffraction spread of a wave of wavelength λ over a propagation distance L [16–18].

For a tapered collimator, the bunch spectrum extends up to $\omega_\sigma = c/\sigma_s$ [19], so the relevant reduced wavelength is $\lambda_\sigma/2\pi = c/\omega_\sigma = \sigma_s$; the propagation distance is the taper length L; and the aperture is the transverse footprint of the beam field where it meets the outer wall, i.e., the induced image-charge distribution. We therefore introduce an effective Fresnel number, defined per transverse

projection,

$$N_F = \frac{\langle x^2 \rangle_{\rm im}}{\sigma_s L}, \tag{4}$$

where $\langle \cdots \rangle_{\rm im}$ is the average over the image charge. Using the reduced wavelength gives $N_F = 2\pi N_F^{\rm opt}$; this constant factor is absorbed into the numerical coefficient of the taper law. Figure 3 illustrates the corresponding image-charge distributions.

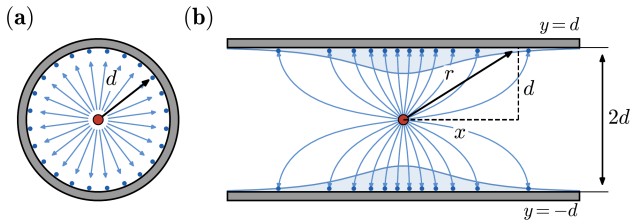


FIG. 3. Illustration of the image-charge distributions used in the Fresnel number interpretation. (a) Round pipe of radius d, the image charge is uniformly distributed around the circumference, giving $\langle x^2 \rangle_{\rm im} = d^2/2$ for one transverse projection. (b) Two parallel plates at $y = \pm d$ in the wide plate limit, $W \gg d$. The image charge is concentrated on the two plates, giving $\langle x^2 \rangle_{\rm im} = d^2$.

For the round geometry, we approximate the image charge as uniformly distributed around the circular boundary at $r = d$. For one transverse projection, $x = d\cos\theta$, and the corresponding mean-square transverse extent is

$$\langle x^2 \rangle_{\rm im}^{\rm rnd} = \frac{d^2}{2\pi} \int_0^{2\pi} \cos^2\theta \, d\theta = \frac{d^2}{2}. \tag{5}$$

Using this effective transverse scale in the Fresnel parameter gives

$$N_F^{\rm rnd} = \frac{\langle x^2 \rangle_{\rm im}^{\rm rnd}}{\sigma_s L} = \frac{d^2}{2\sigma_s L}. \tag{6}$$

For the flat geometry with $W \gg d$, the image charge is distributed over the plates at $y = \pm d$. The Green's function between two grounded parallel plates is given by the monopole potential in Eq. (29) of Ref. [11],

$$\phi_m(x,y) = \ln \frac{\cosh u + \cos v}{\cosh u - \cos v}, \qquad u = \frac{\pi x}{2d}, \quad v = \frac{\pi y}{2d}. \tag{7}$$

On the upper plate, $y = d$ and therefore $v = \pi/2$. The normal derivative is

$$\left. \frac{\partial \phi_m}{\partial y} \right|_{y=d} = -\frac{\pi}{d} \operatorname{sech}\left(\frac{\pi x}{2d}\right), \tag{8}$$

The corresponding induced surface charge density on each plate is

$$\Sigma(x) = -\frac{1}{4d} \operatorname{sech}\left(\frac{\pi x}{2d}\right), \tag{9}$$

with $\int_{-\infty}^{\infty} \Sigma(x)\, dx = -1/2$. The transverse extent of this image-charge distribution is characterized by its second moment,

$$\langle x^2 \rangle_{\rm im}^{\rm flt} = \frac{\displaystyle\int_{-\infty}^{\infty} x^2 \Sigma(x)\, dx}{\displaystyle\int_{-\infty}^{\infty} \Sigma(x)\, dx} = \frac{\displaystyle\int_{-\infty}^{\infty} x^2 \operatorname{sech}\left(\frac{\pi x}{2d}\right) dx}{\displaystyle\int_{-\infty}^{\infty} \operatorname{sech}\left(\frac{\pi x}{2d}\right) dx}. \tag{10}$$

With the substitution $t = \pi x/(2d)$, the denominator and nominator of Eq. (10) becomes $\int_{-\infty}^{\infty} \operatorname{sech}\left(\frac{\pi x}{2d}\right) dx = 2d$, and

$$\int_{-\infty}^{\infty} x^2 \operatorname{sech}\left(\frac{\pi x}{2d}\right) dx = \left(\frac{2d}{\pi}\right)^3 \int_{-\infty}^{\infty} t^2 \operatorname{sech}(t)\, dt. \tag{11}$$

Using the standard integral $\int_{-\infty}^{\infty} t^2 \operatorname{sech}(t)\, dt = \frac{\pi^3}{4}$, we get, $\int_{-\infty}^{\infty} x^2 \operatorname{sech}\left(\frac{\pi x}{2d}\right) dx = 2d^3$. Therefore, Eq. (10) becomes $\langle x^2 \rangle_{\rm im}^{\rm flt} = d^2$. The corresponding Fresnel number is

$$N_F^{\rm flt} = \frac{d^2}{\sigma_s L}. \tag{12}$$

From Eq. (6) and Eq. (12), we obtain,

$$N_F^{\rm flt} = 2N_F^{\rm rnd}. \tag{13}$$

With the corresponding Fresnel number definitions, the arguments of the round and flat taper functions become $0.4N_F^{\rm rnd}$ and $0.4N_F^{\rm flt}$, respectively. The taper law can therefore be written as a single geometry-independent expression,

$$\frac{k_{\parallel,\rm tpr}^{\rm opt}(\sigma_s)}{k_{\parallel,\rm step}(\sigma_s)} \simeq \left[\frac{2}{\pi} \tan^{-1}(0.4N_F)\right]^2, \tag{14}$$

where N_F is the Fresnel number for the corresponding geometry and thus provides a common physical basis for the axisymmetric and rectangular taper scalings.

III. OPTICAL TO INDUCTIVE REGIME TRANSITION

The Fresnel number provides a qualitative measure of the diffraction behavior of the tapered collimator. For $N_F \gg 1$, the loss factor approaches the step value, while for $N_F \leq 1$, diffraction in the taper reduces it according to the arctan law from Eq. (14). Both limits correspond to the optical regime shown in Fig. 2. The onset of the inductive regime is set by the cutoff wavenumber, $\sigma_s > \sigma_i = 1/(\sqrt{2\ln 2}\, k_c)$, independently of N_F. At the transition,

$$N_F^{\rm rnd}(\sigma_i) = \frac{\sqrt{2\ln 2}\, j_{01}}{2} \frac{d}{L} \simeq 1.42 \frac{d}{L}, \tag{15}$$

and

$$N_F^{\rm flt}(\sigma_i) \simeq \frac{\sqrt{2\ln 2}\,\pi}{2}\frac{d}{L} \simeq 1.85\frac{d}{L}, \tag{16}$$

so the inductive regime is reached at $N_F < 1$ only for $d/L \lesssim 0.5$.

The transition from the optical to the inductive regime is characterized by the cutoff wavenumber of the lowest relevant longitudinal mode. Figure 4 illustrates the electromagnetic field distributions of the TM_{01} mode in a circular waveguide and the TM_{11} mode in a rectangular waveguide. For the round geometry, the cutoff wavenumber of the TM_{01} mode is given by

$$k_c^{\rm rnd} = \frac{j_{01}}{d} = \frac{2.405}{d}, \tag{17}$$

where $j_{01} = 2.405$ is the first zero of the Bessel function J_0.

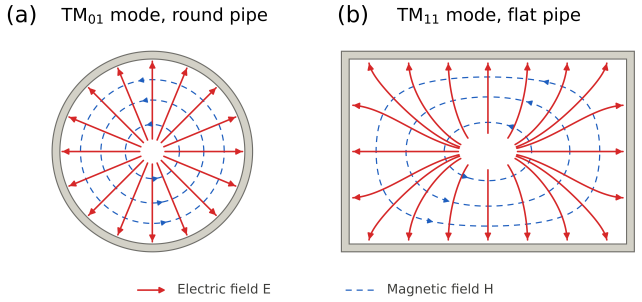


FIG. 4. Electromagnetic field distributions in the pipe cross-section for the lowest-order TM modes: (a) the TM_{01} mode in a round geometry and (b) the TM_{11} mode in a flat geometry. Red solid and blue dashed arrows denote the electric field and magnetic field, receptively.

To relate the modal scale to the rms bunch length, we use the half-maximum point of a Gaussian distribution. For a Gaussian bunch, $\lambda(z)/\lambda(0) = \exp[-z^2/(2\sigma_i^2)]$. At half maximum, $\lambda(z)/\lambda(0) = 1/2$, which gives $N = z/\sigma_i = \sqrt{2\ln 2}$.

For the axisymmetric collimator, the characteristic modal length is $z_c^{\rm rnd} = 1/k_c^{\rm rnd}$. Associating this scale with the Gaussian half-maximum scale gives $N\sigma_{\rm i}^{\rm rnd} = 1/k_c^{\rm rnd}$. Therefore,

$$\sigma_{\rm i}^{\rm rnd} = \frac{1}{Nk_c^{\rm rnd}} = \frac{d}{Nj_{01}}. \tag{18}$$

For the rectangular collimator, the cutoff wavenumber is written as

$$k_c^{\rm flt} = \pi\sqrt{\left(\frac{m}{W}\right)^2 + \left(\frac{n}{2d}\right)^2}. \tag{19}$$

We consider the TM_{11} mode of a rectangular waveguide with full width W and full height $2d$, where $m = 1$ and $n = 1$. The corresponding modal length is $z_c^{\rm flt} = 1/k_c^{\rm flt}$. Using the same Gaussian half-maximum condition, $N\sigma_{\rm i}^{\rm flt} = 1/k_c^{\rm flt}$, which gives

$$\sigma_{\rm i}^{\rm flt} = \frac{1}{Nk_c^{\rm flt}} = \frac{1}{N\pi\sqrt{\left(\frac{1}{W}\right)^2 + \left(\frac{1}{2d}\right)^2}}. \tag{20}$$

Thus $\sigma_i \propto 1/k_c$ provides the characteristic scale separating the optical and inductive branches of the tapered collimator.

IV. TWO-REGIME LOSS FACTOR MODEL OF TAPERED COLLIMATORS

We first consider the corresponding untapered step collimators, which provide the reference loss factors for the axisymmetric and rectangular geometries. We then extend the analysis to tapered collimators and consider two bunch-length regimes: optical and inductive.

A. Optical Regime

1. *Step*

For an axisymmetric step collimator, the longitudinal impedance is given by [20–22]

$$Z_{\parallel,\rm step}^{\rm rnd} = \frac{4}{c}\ln\left(\frac{d}{b}\right), \tag{21}$$

where b and d are the smaller and larger radii, respectively. For a Gaussian bunch with rms length σ_s, the corresponding loss factor is

$$k_{\parallel,\rm step}^{\rm rnd} = \frac{c}{2\sqrt{\pi}\sigma_s} Z_{\parallel,\rm step}^{\rm rnd}. \tag{22}$$

For the rectangular collimator, the step-transition impedance can be obtained from the optical approximation for a flat aperture [11]. In the wide-flat limit, $W \gg d$, the derivation begins with the monopole potential given in Eq. (29) of Ref. [11] for two parallel conducting plates,

$$\phi_m(x,y) = \ln\left[\frac{\cosh\left(\frac{\pi x}{2d}\right) + \cos\left(\frac{\pi y}{2d}\right)}{\cosh\left(\frac{\pi x}{2d}\right) - \cos\left(\frac{\pi y}{2d}\right)}\right]. \tag{23}$$

At the smaller aperture, $y = b$, and using $\alpha = b/d$, and differentiating Eq. (23) with respect to y gives

$$\frac{\partial\phi_m}{\partial y}(x,b) = -\frac{2\pi}{d}\frac{\cosh\left(\frac{\pi x}{2d}\right)\sin\left(\frac{\pi\alpha}{2}\right)}{\cosh\left(\frac{\pi x}{d}\right) - \cos(\pi\alpha)}. \tag{24}$$

Using Eq. (23), the corresponding potential at $y = b$ is

$$\phi_m(x,b) = \ln\left[\frac{\cosh\left(\frac{\pi x}{2d}\right)+\cos\left(\frac{\pi\alpha}{2}\right)}{\cosh\left(\frac{\pi x}{2d}\right)-\cos\left(\frac{\pi\alpha}{2}\right)}\right]. \quad (25)$$

The longitudinal impedance can then be written as

$$Z_{\parallel,\mathrm{step}}^{\mathrm{flt}} = -\frac{2}{\pi c}\int_0^\infty \phi_m(x,b)\frac{\partial\phi_m}{\partial y}(x,b)\,dx. \quad (26)$$

Substituting Eqs. (24) and (25) into Eq. (26) gives

$$Z_{\parallel,\mathrm{step}}^{\mathrm{flt}} = \frac{4}{dc}\int_0^\infty dx\,\frac{\sin\left(\frac{\pi\alpha}{2}\right)\cosh\left(\frac{\pi x}{2d}\right)}{\cos(\pi\alpha)-\cosh\left(\frac{\pi x}{d}\right)} \times \ln\left[\frac{\cosh\left(\frac{\pi x}{2d}\right)-\cos\left(\frac{\pi\alpha}{2}\right)}{\cosh\left(\frac{\pi x}{2d}\right)+\cos\left(\frac{\pi\alpha}{2}\right)}\right]. \quad (27)$$

Introducing the dimensionless coordinate $x' = x/(2d)$, we obtain

$$Z_{\parallel,\mathrm{step}}^{\mathrm{flt}} = \frac{8}{c}\int_0^\infty dx'\,\frac{\sin\left(\frac{\pi\alpha}{2}\right)\cosh(\pi x')}{\cos(\pi\alpha)-\cosh(2\pi x')} \times \ln\left[\frac{\cosh(\pi x')-\cos\left(\frac{\pi\alpha}{2}\right)}{\cosh(\pi x')+\cos\left(\frac{\pi\alpha}{2}\right)}\right]. \quad (28)$$

Therefore, the loss factor of the flat collimator is

$$k_{\parallel,\mathrm{step}}^{\mathrm{flt}} = \frac{c}{2\sqrt{\pi}\sigma_s}Z_{\parallel,\mathrm{step}}^{\mathrm{flt}}. \quad (29)$$

The corresponding mks unit is obtained by multiplying by $cZ_0/4\pi$, where $Z_0 \approx 376.73\ \Omega$ is the impedance of free space.

2. Tapered

For short bunches, tapering reduces the loss factor relative to the corresponding step collimator. Wakefield simulations with ECHO and GdfidL show that this reduction can be represented by a geometry-dependent taper factor. For axisymmetric collimators with $d-b > b$, ECHO simulations give $\mu_{\mathrm{rnd}} = 0.2$ [2], whereas for wide rectangular collimators with $d-b > b$ and $W \gg d$, GdfidL simulations give $\mu_{\mathrm{flt}} = 0.4$ [3], consistent with Eq. (13).

The optical regime loss factor is

$$k_{\parallel,\mathrm{tpr}}^{\mathrm{opt}}(\sigma_s) = k_{\parallel,\mathrm{step}}(\sigma_s)\left[\frac{2}{\pi}\tan^{-1}\left(\frac{\mu d^2}{\sigma_s L}\right)\right]^2. \quad (30)$$

The optical regime is identified by

$$\sigma_s \le \sigma_i, \quad (31)$$

where σ_i denotes the characteristic bunch length separating the optical and inductive regimes.

B. Inductive Regime

As the bunch length increases beyond σ_i, the bunch spectrum shifts toward lower frequencies and the loss factor departs from the short-bunch optical behavior. The following derivation is based on an asymptotic lowest mode approximation, in which the long bunch response is assumed to be dominated by the lowest relevant electromagnetic mode, characterized by the cutoff wavenumber k_c.

For a Gaussian bunch of rms length σ_s, the loss factor can be expressed in the wavenumber domain as

$$k_\parallel(\sigma_s) = \frac{c}{\pi}\int_0^\infty \mathrm{Re}\big[Z_\parallel(k)\big]\exp\big(-k^2\sigma_s^2\big)\,dk. \quad (32)$$

The factor $\exp(-k^2\sigma_s^2)$ represents the Gaussian spectral weighting of the bunch and increasingly suppresses high wavenumber components as σ_s increases.

Within the asymptotic lowest mode approximation, $\mathrm{Re}[Z_\parallel(k)]$ is taken to vary slowly near the lowest cutoff. The leading bunch-length dependence of the long bunch response can then be approximated by the Gaussian spectral tail above k_c,

$$k_{\parallel,\mathrm{tpr}}^{\mathrm{ind}}(\sigma_s) \propto \int_{k_c}^\infty \exp\big(-k^2\sigma_s^2\big)\,dk. \quad (33)$$

Here, $u = k\sigma_s$, with $dk = du/\sigma_s$, and using the definition of the complementary error function [23, 24], $\mathrm{erfc}(x) = \frac{2}{\sqrt{\pi}}\int_x^\infty e^{-t^2}\,dt$. Eq. (33) becomes

$$k_{\parallel,\mathrm{tpr}}^{\mathrm{ind}}(\sigma_s) \propto \frac{\sqrt{\pi}}{2\sigma_s}\,\mathrm{erfc}(k_c\sigma_s)\,, \quad (34)$$

For sufficiently large $k_c\sigma_s$, the complementar error function has the asymptotic form

$$\mathrm{erfc}(x) \simeq \frac{\exp(-x^2)}{\sqrt{\pi}\,x}, \quad (35)$$

Substituting Eq. (35) into Eq. (34) gives the long-bunch scaling

$$k_{\parallel,\mathrm{tpr}}^{\mathrm{ind}}(\sigma_s) \propto \frac{1}{k_c\sigma_s^2}\exp\big(-k_c^2\sigma_s^2\big)\,. \quad (36)$$

Normalizing Eq. (36) to its value at the characteristic bunch length σ_i for $\sigma_s > \sigma_i$ gives

$$\frac{k_{\parallel,\mathrm{tpr}}^{\mathrm{ind}}(\sigma_s)}{k_{\parallel,\mathrm{tpr}}^{\mathrm{ind}}(\sigma_i)} \simeq \left(\frac{\sigma_i}{\sigma_s}\right)^2\exp\big[-k_c^2\left(\sigma_s^2-\sigma_i^2\right)\big]\,, \quad (37)$$

Matching the inductive branch continuously to the optical branch at $\sigma_s = \sigma_i$, such that $k_{\parallel,\mathrm{tpr}}^{\mathrm{ind}}(\sigma_i) = k_{\parallel,\mathrm{tpr}}^{\mathrm{opt}}(\sigma_i)$, the inductive loss factor is expressed as

$$k_{\parallel,\mathrm{tpr}}^{\mathrm{ind}}(\sigma_s) = k_{\parallel,\mathrm{tpr}}^{\mathrm{opt}}(\sigma_i)\left(\frac{\sigma_i}{\sigma_s}\right)^2\exp\big[-k_c^2\left(\sigma_s^2-\sigma_i^2\right)\big]\,. \quad (38)$$

Using, Eq. (30), the absolute loss factor from Eq. (38) can be writtern as

$$k_{\parallel,\mathrm{tpr}}^{\mathrm{ind}}(\sigma_s) = k_{\parallel,\mathrm{step}}(\sigma_i)\left[\frac{2}{\pi}\tan^{-1}\left(\frac{\mu d^2}{\sigma_i L}\right)\right]^2\left(\frac{\sigma_i}{\sigma_s}\right)^2 \times \exp\left[-k_c^2\left(\sigma_s^2-\sigma_i^2\right)\right]. \tag{39}$$

which is identical to Eq. (2).

From Eq. (22) and (29), the step-transition loss factor is $k_{\parallel,\mathrm{step}} \propto 1/\sigma_s$, therefore

$$\frac{k_{\parallel,\mathrm{step}}(\sigma_i)}{k_{\parallel,\mathrm{step}}(\sigma_s)} = \frac{\sigma_s}{\sigma_i}. \tag{40}$$

From Eqs. (37) and (40), we get

$$\frac{k_{\parallel,\mathrm{tpr}}^{\mathrm{ind}}(\sigma_s)}{k_{\parallel,\mathrm{step}}(\sigma_s)} = \frac{k_{\parallel,\mathrm{tpr}}^{\mathrm{opt}}(\sigma_i)}{k_{\parallel,\mathrm{step}}(\sigma_i)}\left(\frac{\sigma_i}{\sigma_s}\right)\exp\left[-k_c^2\left(\sigma_s^2-\sigma_i^2\right)\right]. \tag{41}$$

At the transition point, the optical branch of Eq. (30) gives $k_{\parallel,\mathrm{tpr}}^{\mathrm{opt}}(\sigma_i)/k_{\parallel,\mathrm{step}}(\sigma_i) = \left[\frac{2}{\pi}\tan^{-1}\left(\frac{\mu d^2}{\sigma_i L}\right)\right]^2$. Hence, for $\sigma_s > \sigma_i$, the inductive branch of the normalized two-regime model is

$$\frac{k_{\parallel,\mathrm{tpr}}^{\mathrm{ind}}(\sigma_s)}{k_{\parallel,\mathrm{step}}(\sigma_s)} = \left[\frac{2}{\pi}\tan^{-1}\left(\frac{\mu d^2}{\sigma_i L}\right)\right]^2\left(\frac{\sigma_i}{\sigma_s}\right) \times \exp\left[-k_c^2\left(\sigma_s^2-\sigma_i^2\right)\right]. \tag{42}$$

C. Combined Optical–Inductive Model

Using the optical result of Eq. (30) together with the long-bunch result of Eq. (38), the absolute loss factor of the tapered structure can be written as

$$k_{\parallel,\mathrm{tpr}}(\sigma_s) = \begin{cases} k_{\parallel,\mathrm{tpr}}^{\mathrm{opt}}(\sigma_s), & \sigma_s \le \sigma_i \\ & \text{(optical)} \\ k_{\parallel,\mathrm{tpr}}^{\mathrm{opt}}(\sigma_i)\left(\dfrac{\sigma_i}{\sigma_s}\right)^2 & \sigma_s > \sigma_i \\ \quad \times \exp\left[-k_c^2\left(\sigma_s^2-\sigma_i^2\right)\right], & \text{(inductive)} \end{cases} \tag{43}$$

The two branches are continuous at $\sigma_s = \sigma_i$. The absolute inductive branch contains $(\sigma_i/\sigma_s)^2$, whereas the corresponding normalized form introduced in Eq. (42) contains σ_i/σ_s because $k_{\parallel,\mathrm{step}} \propto 1/\sigma_s$. This formulation connects the short-bunch optical behavior to the long-bunch inductive regime within a single loss factor model.

D. Frequency and Catch-Up Distance Conditions

The conventional optical approximation is associated with two main conditions: the bunch spectrum must extend to sufficiently high frequencies, and the transition length must be short compared with the catch-up distance [11]. We examine both conditions for the tapered collimators considered here.

The taper angle is written as $\theta_{\mathrm{taper}} = (d-b)/L$ [25, 26]. The corresponding characteristic frequency is

$$f_{\mathrm{taper}} = \frac{c}{2\pi b\theta_{\mathrm{taper}}}. \tag{44}$$

For $b = 4.6$ mm, $d = 18$ mm, and $L = 300$ mm, $f_{\mathrm{taper}} \simeq 232$ GHz; thus, the high frequency condition for the optical approximation requires frequencies well above this characteristic scale.

The second condition is determined by the catch-up distance that is used to determine whether the electromagnetic field generated at transition can interact with the bunch within the tapered region. For a Gaussian bunch with characteristic angular frequency [16] is $\omega \simeq c/\sigma_s$, the catch-up distance can be written as [27]

$$L_{\mathrm{catch}} = \frac{b^2\omega}{c} = \frac{b^2}{\sigma_s}. \tag{45}$$

The conventional short transition condition is $L < L_{\mathrm{catch}}$ [11]. For sufficiently short bunches, L_{catch} is large and this condition is satisfied. As the bunch length increases, $L_{\mathrm{catch}} \propto 1/\sigma_s$ decreases and can become smaller than the taper length.

Using the Fresnel number scaling introduced above, $N_F \sim d^2/(\sigma_s L)$, together with $L_{\mathrm{catch}} \sim b^2/\sigma_s$, the ratio of the catch-up distance to the taper length can be expressed as

$$\frac{L_{\mathrm{catch}}}{L} \sim N_F\left(\frac{b}{d}\right)^2. \tag{46}$$

Near $N_F \sim 1$, this ratio therefore scales as $(b/d)^2$. For a sufficiently large change in aperture, such as $d-b > b$ [3], corresponding to $d > 2b$, the ratio is reduced accordingly, and the catch-up distance can become shorter than the taper length, $L_{\mathrm{catch}} < L$.

The wakefield simulations nevertheless show that the loss factor can continue to follow the short bunch optical scaling even when $L_{\mathrm{catch}} < L$. Thus, the conventional catch-up distance condition alone does not provide a sharp boundary for the optical regime. This behavior is consistent with the Fresnel number interpretation discussed above. In the present model, the cutoff wavenumber, k_c determines the characteristic bunch length separating the optical and inductive branches, with $\sigma_i \propto 1/k_c$.

V. RESULTS AND DISCUSSION

Unless otherwise stated, the reference parameters used in the parametric analysis are listed in Table I. When studying the dependence on a particular parameter, that parameter is varied while all other parameters are kept at their reference values.

TABLE I. Reference parameters and characteristic bunch-length scales.

Parameter	Round	Flat
Small radius/aperture, b	4.6 mm	4.6 mm
Large radius/aperture, d	18 mm	18 mm
Taper length, L	300 mm	300 mm
Gap, g	100 mm	100 mm
Chamber width, W	–	67 mm
Optical–inductive transition, σ_i	6.34 mm	8.55 mm

A. Longitudinal Wakefield Simulation

We performed numerical simulations using both ECHO and GdfidL for the flat tapered collimator. For the flat geometry, b and d denote the smaller and larger vertical half-apertures, respectively, while W is the full chamber width. The longitudinal wake potential $W_\parallel(s)$ is calculated for a Gaussian bunch with rms length σ_s.

For a finite bunch, the longitudinal wake potential is obtained by convolving the point charge wake function $w_\parallel(s)$ with as $W_\parallel(s) = \int_{-\infty}^{\infty} w_\parallel(s-s')\lambda(s')\,ds'$, where $\lambda(s)$ is the normalized longitudinal distribution with $\int_{-\infty}^{\infty}\lambda(s)\,ds = 1$. We obtain $W_\parallel(s)$ directly from wakefield simulations for the specified Gaussian bunch. The corresponding longitudinal loss factor is then evaluated in the wake domain as $k_\parallel = -\int_{-\infty}^{\infty} W_\parallel(s)\lambda(s)\,ds$, where the sign convention is chosen such that $k_\parallel > 0$ corresponds to energy loss by the bunch.

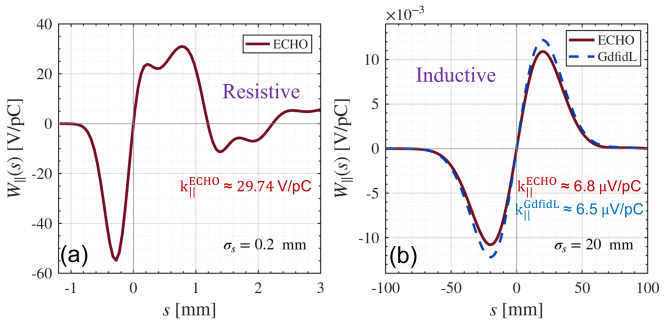


FIG. 5. Simulated longitudinal wakefields for two bunch lengths: (a) short bunch ($\sigma_s = 0.2$ mm), exhibiting a predominantly resistive response obtained using ECHO; and (b) long bunch ($\sigma_s = 20$ mm), exhibiting a predominantly inductive response obtained using ECHO and GdfidL..

Figure 5 shows the longitudinal wakefields of the flat collimator simulated with ECHO and GdfidL. Two bunch lengths are selected to illustrate the resistive and inductive responses [28]. For the short bunch ($\sigma_s = 0.2$ mm), the wakefield calculated with ECHO exhibits oscillations and a loss factor of $k_{\parallel,\mathrm{tpr}} = 29.74$ V/pC, indicating a predominantly resistive response. In contrast, for the long bunch ($\sigma_s = 20$ mm), the wakefield shows a nearly antisymmetric bipolar profile, with a substantially reduced loss factors of $k_{\parallel,\mathrm{tpr}} \approx 6.8$ μV/pC and 6.5 μV/pC obtained from ECHO and GdfidL, respectively, indicating a predominantly inductive response with negligible net energy loss. The small difference between the numerical results may arise from the chosen step sizes of both codes, and the GdfidL results, obtained with a 50 μm step size, are expected to converge toward the ECHO results as the step size of GdfidL is further reduced.

B. Normalized Loss Factor Scaling

We present the numerical results for the round and flat tapered collimators in normalized form to examine the geometrical scaling and directly compare them with the analytical model in the optical and inductive regimes.

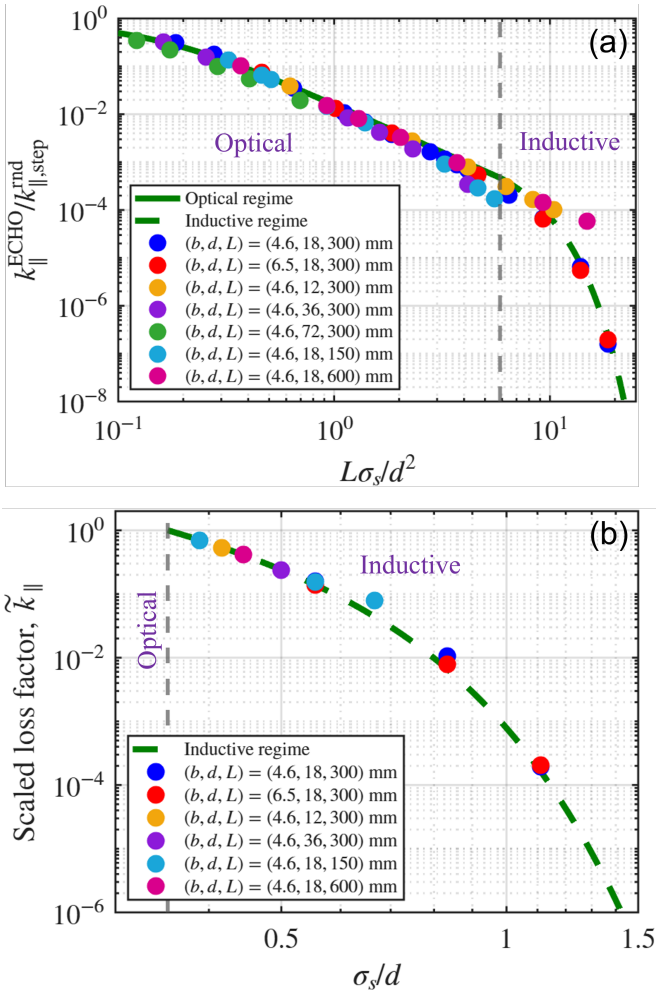


FIG. 6. Normalized loss factor of the round tapered collimator: (a) optical regime and (b) inductive regime. The symbols represent numerical results obtained using ECHO. The vertical dashed lines indicate the optical-inductive transition σ_i^{rnd}.

For the round tapered collimator, the reference geometry is $b = 4.6$ mm, $d = 18$ mm, and $L = 300$ mm. Additional geometries are considered by individually varying b to 6.5 mm, d to 12, 36, and 72 mm, and L to 150

and 600 mm, respectively, while keeping the remaining parameters fixed. In Fig. 6(a), the numerical loss factor is normalized by the step loss factor of Eq. (22) as $k_{\parallel}^{\mathrm{ECHO}}/k_{\parallel,\mathrm{step}}^{\mathrm{rnd}}$ and plotted against the scaled bunch length $L\sigma_s/d^2$. The analytical data from Eq. (30) are plotted as the ratio of the tapered collimator loss factor to the corresponding step loss factor for different bunch lengths (solid green curve). The numerical results for the different geometries follow a common trend and agree well with the analytical predictions in the optical regime.

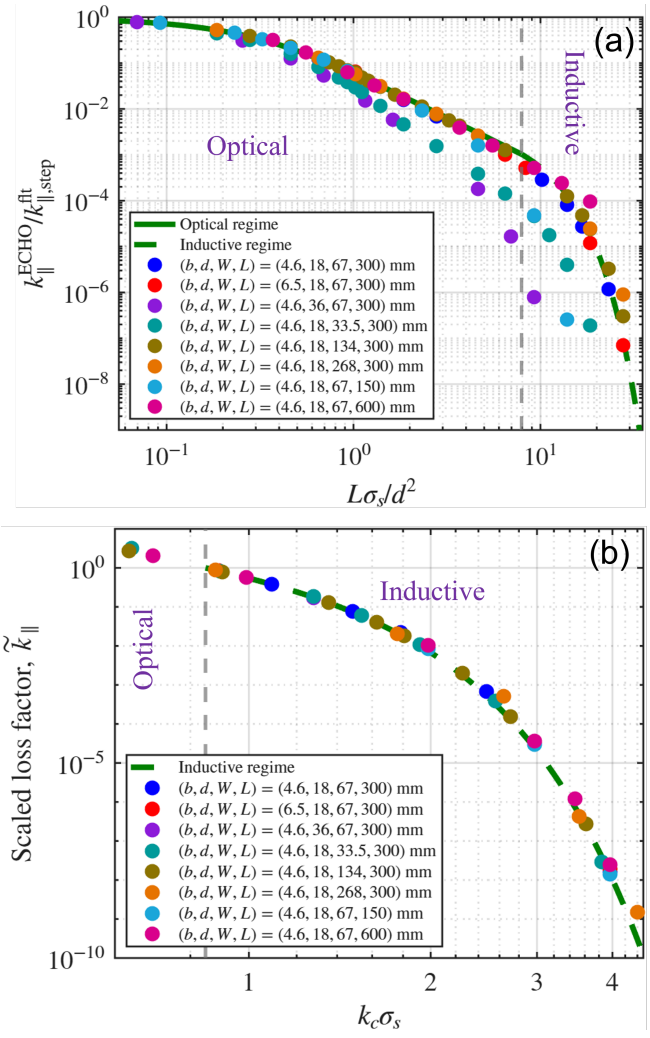


FIG. 7. Normalized loss factor of the flat tapered collimator: (a) optical regime and (b) inductive regime. The symbols represent numerical results obtained using ECHO. The vertical dashed lines indicate the optical-inductive transition σ_i^{flt}.

Figure 6(b) shows the inductive regime results as a function of the scaled bunch length σ_s/d. The vertical axis represents the scaled loss factor $\widetilde{k}_{\parallel}(\sigma_s) = [k_{\parallel}^{\mathrm{ECHO}}(\sigma_s)/k_{\parallel}^{\mathrm{ECHO}}(\sigma_j)]U_{\mathrm{rnd}}(r_j)$, where $r = \sigma_s/d$, σ_j is the first simulated bunch length satisfying $\sigma_j \geq \sigma_i$, $r_j = \sigma_j/d$, $r_i = \sigma_i/d$. The analytical data is represented by $U_{\mathrm{rnd}}(r) = (r_i/r)^2 \exp[-j_{01}^2(r^2 - r_i^2)]$ (dashed green curve). The scaled numerical results follow the predicted inductive decay for longer bunches.

For the flat tapered collimator, we use the reference geometry $b = 4.6$ mm, $d = 18$ mm, $W = 67$ mm, and $L = 300$ mm. We apply the same variations in b, d, and L as in the round geometry and additionally vary the chamber width to $W = 33.5$, 134, and 268 mm, respectively. In Fig. 7(a), the numerical loss factor is normalized by the step loss factor of Eq. (29) as $k_{\parallel}^{\mathrm{ECHO}}/k_{\parallel,\mathrm{step}}^{\mathrm{flt}}$ and plotted against $L\sigma_s/d^2$. The analytical predictions from Eq. (39), normalized by $k_{\parallel,\mathrm{step}}^{\mathrm{flt}}$, are also plotted (solid green curve). The numerical results for the different geometries follow a common trend in the optical regime, while the influence of the finite chamber width becomes more pronounced toward the inductive regime. The larger deviations for $W = 33.5$ mm, $d = 18$ mm and $W = 67$ mm, $d = 36$ mm arise from their transverse aspect ratios. In both cases, $W/(2d) \approx 1$, so the cross section approaches a square rather than a wide flat rectangle. The corresponding transverse image-charge distribution therefore differs from the wide flat limit underlying the analytical approximation, resulting in larger discrepancies between the analytical model and the numerical results.

To include the finite transverse scale, the inductive-regime results are plotted in Fig. 7(b) using $u = k_c\sigma_s$, where $k_c = \pi\sqrt{1/W^2 + 1/(2d)^2}$. The vertical axis represents the scaled loss factor $\widetilde{k}_{\parallel}(\sigma_s) = [k_{\parallel}^{\mathrm{ECHO}}(\sigma_s)/k_{\parallel}^{\mathrm{ECHO}}(\sigma_j)]U_{\mathrm{flt}}(u_j)$, where σ_j is the first simulated bunch length satisfying $\sigma_j \geq \sigma_i$, $u_j = k_c\sigma_j$, $u_i = k_c\sigma_i$. The analytical results are presented by $U_{\mathrm{flt}}(u) = (u_i/u)^2 \exp[-(u^2 - u_i^2)]$ (dashed green curve). As k_c incorporates both the vertical half-aperture d and the finite width W, the geometry dependence is captured by the scaled variable u. The vertical normalization further removes differences in the overall amplitude, allowing the different flat geometries to follow a common inductive trend.

C. Parametric Analysis of Round and Flat Structure

We systematically investigate the dependence of the loss factor and regime boundaries on b, d, and L for round collimators, while also considering the chamber width W for flat collimators. Figure 8(a) shows the dependence of the loss factor of the round collimator on the large radius d for fixed $b = 4.6$ mm and $L = 300$ mm. The transition bunch length scales linearly with the large radius, $\sigma_i^{\mathrm{rnd}} \propto d$. For $d = 12$, 18, 36, and 72 mm, the corresponding transition bunch lengths are $\sigma_i^{\mathrm{rnd}} \approx 4.23$, 6.34, 12.69, and 25.37 mm, respectively. Thus, increasing d shifts the optical inductive transition toward larger bunch lengths. The geometries considered here also satisfy the condition $d - b > b$ [3]. Figure 8(b) shows the effects of the small radius b and taper length L for fixed $d = 18$ mm. Since σ_i^{rnd} depends only on d, varying b or L does not shift the

transition, which remains at $\sigma_i^{\mathrm{rnd}} \approx 6.34$ mm. Increasing the taper length reduces the loss factor, corresponding to weaker beam coupling for a more gradual transition [3].

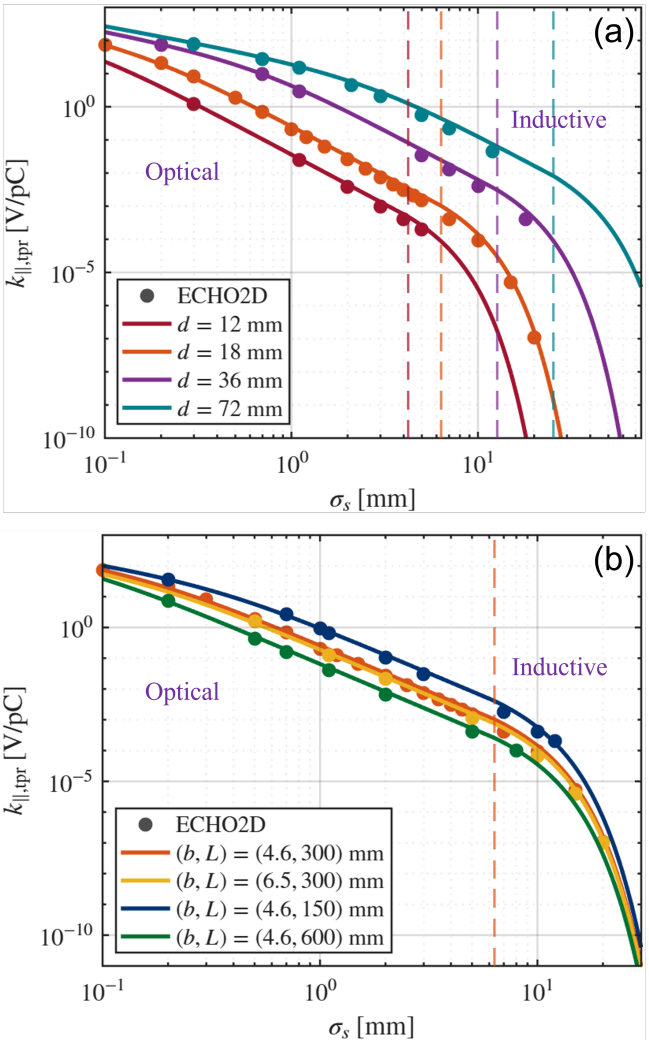


FIG. 8. Dependence of the loss factor of the round tapered collimator on the geometrical parameters: (a) variation of d for fixed $b = 4.6$ mm and $L = 300$ mm; (b) variation of b and L for fixed $d = 18$ mm. The symbols represent numerical results obtained using ECHO. The vertical dashed lines indicate the optical-inductive transition σ_i^{rnd}.

Figure 9(a) shows the dependence of the loss factor of flat collimator on b, d, and L for a fixed chamber width $W = 67$ mm. For $d = 18$ and 36 mm, the corresponding transition bunch lengths are $\sigma_i^{\mathrm{flat}} \approx 8.55$ and 13.23 mm, respectively. Thus, increasing d shifts the optical inductive transition toward longer bunch lengths. In contrast, varying b or L does not shift σ_i^{flat}, since the transition depends only on d and W. Increasing the taper length reduces the loss factor [3], corresponding to a more gradual geometrical transition. Figure 9(b) shows the effect of the chamber width W for fixed $b = 4.6$ mm, $d = 18$ mm, and $L = 300$ mm. For $W = 33.5$, 67, 134, and 268 mm, the corresponding transition bunch lengths are $\sigma_i^{\mathrm{flat}} \approx 6.62$, 8.55, 9.38, and 9.62 mm, respectively. Increasing W decreases the cutoff wavenumber and shifts the transition toward longer bunch lengths.

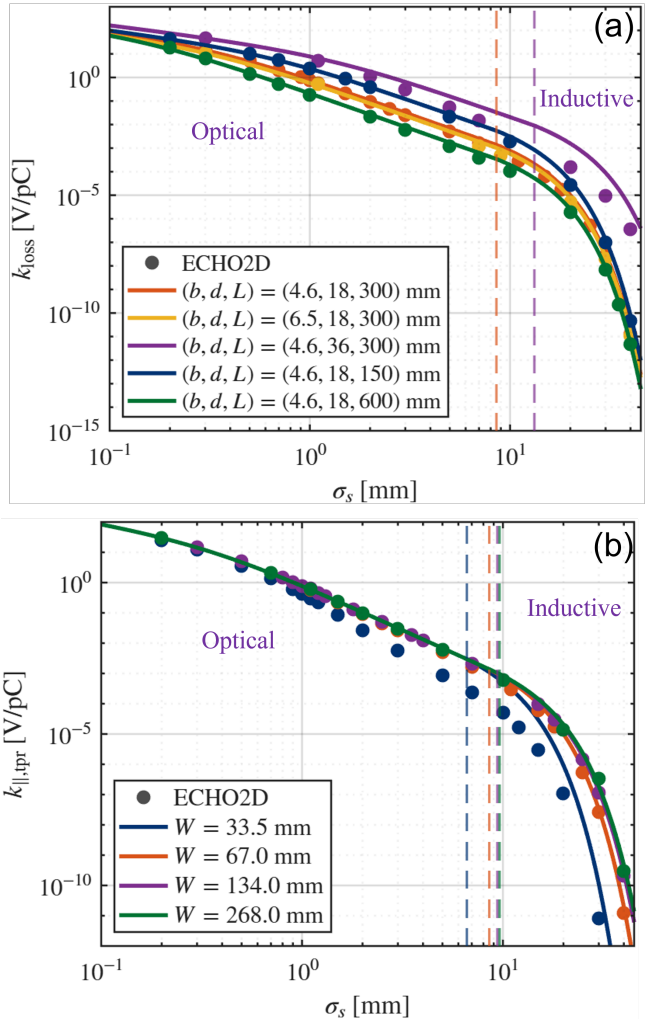


FIG. 9. Dependence of the loss factor of the flat tapered collimator on the geometrical parameters: (a) variation of b, d, and L for fixed chamber width $W = 67$ mm; (b) variation of W for fixed $b = 4.6$ mm, $d = 18$ mm, and $L = 300$ mm. The symbols represent numerical results obtained using ECHO. The vertical dashed lines indicate the optical-inductive transition σ_i^{flat}.

The analytical flat chamber model is derived under the wide chamber assumption, for which $W > 2d$. The numerical results indicate that quantitative agreement improves further when the chamber is sufficiently wide that the side walls carry only a small fraction of the image charge. This condition is approximately satisfied for $W \gtrsim 3.6d$, or equivalently $W/(2d) \gtrsim 1.8$. For narrower chambers, neglecting the finite width can overestimate the loss factor by up to an order of magnitude. This limitation is evident in Fig. 9(a), where $d = 36$ mm gives $2d = 72$ mm, exceeding the fixed width $W = 67$ mm.

Similarly, in Fig. 9(b), the case $W = 33.5$ mm is narrower than $2d = 36$ mm for $d = 18$ mm. In both cases, the wide chamber assumption is violated, resulting in larger discrepancies between the analytical model and the numerical results. These deviations are therefore associated primarily with finite width effects rather than with the optical to inductive transition scaling.

D. Comparison of Axisymmetric and Flat Structures

We compare the loss factors of the round and flat tapered collimators for $b = 4.6$ mm, $d = 18$ mm, and $L = 300$ mm, with $W = 67$ mm for the flat geometry shown in Fig. 10. The geometry dependent parameters $\mu_{\rm rnd} = 0.2$ and $\mu_{\rm flat} = 0.4$, originally introduced for the optical regime [2, 3], are retained in the combined optical-inductive regime model. The dependence of the taper correction on $d^2/(\sigma_s L)$ is consistent with Fresnel number scaling (Eq. (13)), supporting the use of these parameters across the optical to inductive transition.

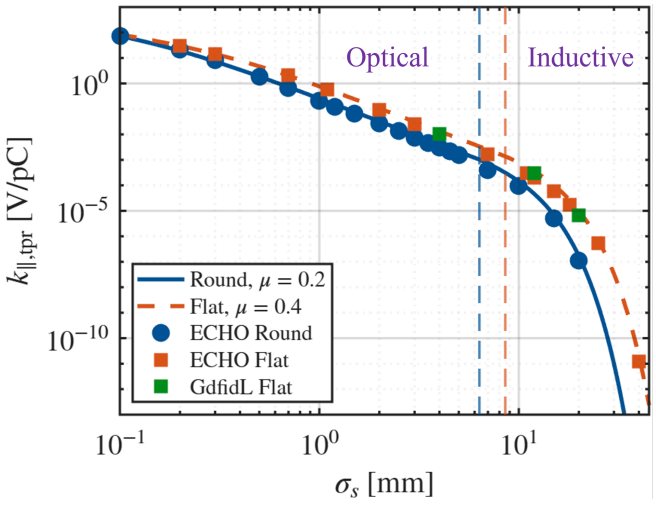


FIG. 10. Comparison of the loss factors for round and flat tapered collimators. Symbols show the simulation results obtained with ECHO for round collimator and with ECHO and GdfidL for flat collimator. The vertical dashed lines indicate the inductive transition bunch lengths, $\sigma_i^{\rm rnd} = 6.36$ mm and $\sigma_i^{\rm flt} = 8.57$ mm.

At $\sigma_s = 0.2$ mm, in the optical regime, ECHO gives loss factors of 29.74 and 20.7 V/pC for the flat and round collimators, respectively, compared with 29.8 and 19.1 V/pC from Eq. (43). At $\sigma_s = 20$ mm, in the inductive regime, the ECHO values decrease to 6.85 and 0.110 μV/pC for flat and round collimators, while the model predicts 10.1 and 0.167 μV/pC, respectively. For the flat structure at $\sigma_s = 20$ mm, GdfidL gives 6.5 μV/pC, in good agreement with ECHO. These results demonstrate the rapid reduction in loss factor for longer bunches, with the model capturing the overall trend across both geometries.

E. Lessons Learned: Detecting Geometry Errors in Simulation Input Models

Wakefield simulations of collimators are often based on geometry files taken directly from the engineering design, where errors in the jaw position are not always apparent. Figure 11 shows such a case for the ESR vertical collimator. In the initial input model the whole jaw assembly was displaced vertically with respect to the standard rectangular beam pipe, while the minimum jaw separation $\Delta = 2b$ and the overall height H were preserved. As a result, the upper and lower halves of the collimator have different effective half-apertures $d \pm \delta$ and $b \pm \delta$, and the junctions between the displaced chamber and the beam pipe form untapered steps of height δ. While the tapered jaws suppress the loss factor through the factor $[(2/\pi)\tan^{-1}(\mu d^2/\sigma_s L)]^2$, these steps are not tapered and contribute the full step loss. For long bunches they therefore dominate, and the simulated loss factor exceeds the prediction of Eq. (43) by a large factor, far beyond the model uncertainty. The comparison with Eq. (43) thus immediately identifies the inconsistency in the input model; after the jaw assembly was restored to its symmetric position, the simulated loss factor agreed with Eq. (43).

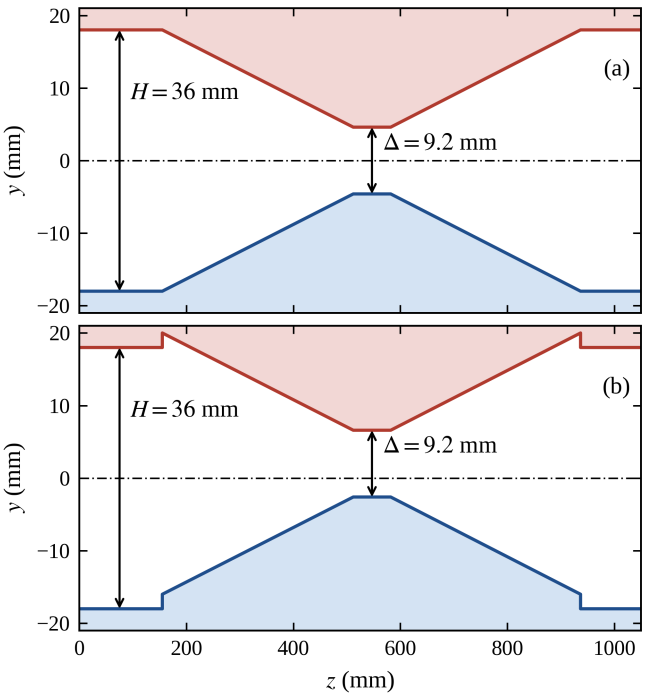


FIG. 11. Geometry verification of the vertical collimator: (a) nominal symmetric jaw configuration and (b) vertically offset jaw configuration with reduced lower clearance. The overall vertical dimension is $H = 36$ mm, and the minimum jaw separation is $\Delta = 9.2$ mm. The red and blue profiles represent the upper and lower jaw surfaces, respectively, while the dashed line indicates the $y = 0$ reference plane.

VI. APPLICATION TO THE EIC ESR COLLIMATOR

The collimators of the EIC Electron Storage Ring (ESR) are designed with movable jaws. At high beam energy the jaws are going to be set closer to the beam, so the choice of material for the jaw tip becomes an important part of the design [29, 30]. Here we consider only the geometric loss factor, due to the change in cross-section, assuming perfectly conducting walls; the resistive-wall contribution of the jaw-tip material is not included.

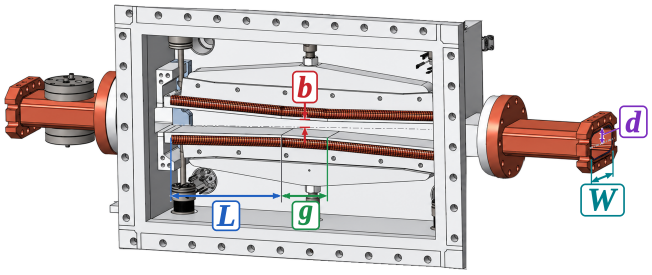


FIG. 12. Three-dimensional model of the EIC ESR flat collimator, showing the opposing tapered jaws, vacuum chamber, and beam-pipe connections.

Figure 12 shows the preliminary design of the vertical collimator. The geometry is characterized by $W = 67$ mm, $d = 18$ mm, $b = 4.6$ mm, $L = 300$ mm and $g = 100$ mm, which are the chamber width, the maximum and minimum vertical half-apertures, the taper length and the length of the narrow straight section, respectively. Two vertical collimators with minimum vertical half-apertures of 4.6 mm and 6.5 mm are planned for operation at 9 GeV.

We use Eq. (43) to determine the loss factor, $k_{\parallel,\mathrm{tpr}}$ of the flat tapered collimator. For the nominal rms bunch length $\sigma_s = 7$ mm we have $N_F = d^2/(\sigma_s L) \approx 0.15$ and $\sigma_s < \sigma_i = 8.6$ mm, so the collimator operates in the optical regime, where the loss factor depends on $d^2/(\sigma_s L)$ and not on b. The minimum half-aperture enters only through the step loss factor $k_{\parallel,\mathrm{step}}(\alpha)$, $\alpha = b/d$. As a result, the loss factor changes only moderately with the jaw setting: $k_{\parallel,\mathrm{tpr}} = 2.5$ mV/pC for $b = 4.6$ mm and 1.9 mV/pC for $b = 6.5$ mm.

At 9 GeV, the ESR stores an average beam current of $I_{\mathrm{avg}} = 2.5$ A in $M = 1160$ bunches, with a bunch charge of $q_b = 28$ nC, and a revolution period of $T_0 = 12.8$ μs. Assuming negligible multibunch wakefield interactions [6], Eq. (43) yields power losses [7] of $P_{\mathrm{loss}} = k_{\parallel,\mathrm{tpr}} I_{\mathrm{avg}}^2 T_0/M = 173$ W and 129 W for $b = 4.6$ mm and $b = 6.5$ mm, respectively, at $\sigma_s = 7$ mm. Resistive-wall losses have been analyzed separately in Ref. [30].

VII. CONCLUSION

In our earlier studies, we obtained a phenomenological expression for the loss factor of axisymmetric tapered collimators from numerical simulations [2] and subsequently extended it to rectangular geometries [3]. Two unexpected features were the dependence of the arctangent scaling parameter $\mu d^2/(\sigma_s L)$ on the larger aperture d, rather than the minimum aperture b, and the factor of two between the coefficients for axisymmetric and rectangular geometries. In the present work, we have provided a physical explanation for these observations. The Fresnel number interpretation clarifies the geometrical scaling, while the combination of diffraction theory and the electrodynamics of the beam-induced image charge explains the difference between the two geometries.

An important result of this work is the establishment of a loss-factor description for rectangular tapered collimators of finite chamber width and the extension of the phenomenological formulation from the optical to the inductive regime for both axisymmetric and rectangular geometries. In the optical limit, the loss factor of an abrupt step is described by the analytical expression derived by Bane, Stupakov and Zagorodnov [11], whereas the reduction associated with tapering is represented by the phenomenological arctangent function. The extension to longer bunches is obtained using an analytical approximation based on the cutoff wavenumber of the lowest relevant electromagnetic mode. Interestingly, the larger aperture d determines the characteristic scale in both the Fresnel-number description and the inductive approximation.

The resulting semi-analytical expression (Eq. (43)) combines the analytical descriptions of the optical and inductive limits with the phenomenological reduction factor for a tapered transition. It provides a continuous description of the loss factor over a broad range of bunch lengths and geometrical parameters, in good agreement with ECHO and GdfidL simulations. Although the present analysis explains the geometrical scaling and the difference between axisymmetric and rectangular collimators, the specific arctangent dependence remains a numerical observation. An analytical derivation of this functional form from Maxwell's equations remains an open problem and would provide a more complete theoretical understanding of the loss factor of tapered structures.

ACKNOWLEDGMENTS

This work was supported by Brookhaven Science Associates, LLC under Contract No. DE-SC0012704 with the U.S. Department of Energy. We are grateful to Michael Blaskiewicz for insightful discussions and guidance throughout this work. We thank Igor Zagorodnov for making the ECHO code available for our use. We also thank Warner Bruns for his valuable advice and assistance with GdfidL.

[1] F. Willeke *et al.*, *Electron Ion Collider Conceptual Design Report 2021*, Tech. Rep. BNL-221006-2021-FORE (Brookhaven National Laboratory, Upton, NY, 2021).

[2] A. Blednykh and S. Krinsky, Physical Review Special Topics - Accelerators and Beams **13**, 064401 (2010).

[3] A. Blednykh and S. Krinsky, in *Proceedings of the 2011 Particle Accelerator Conference (PAC'11)* (New York, NY, USA, 2011) pp. 1816–1818.

[4] A. Blednykh, G. Bassi, V. Smaluk, and R. Lindberg, Physical Review Accelerators and Beams **24**, 104801 (2021).

[5] G. Stupakov, K. L. F. Bane, and I. Zagorodnov, Physical Review Special Topics - Accelerators and Beams **10**, 054401 (2007).

[6] L. Palumbo, V. G. Vaccaro, and M. Zobov, in *CAS – CERN Accelerator School: Advanced Accelerator Physics*, CERN 95-06 (Geneva, 1995) pp. 331–390.

[7] A. W. Chao, *Physics of Collective Beam Instabilities in High Energy Accelerators* (John Wiley & Sons, New York, 1993).

[8] B. W. Zotter and S. A. Kheifets, *Impedances and Wakes in High-Energy Particle Accelerators* (World Scientific, 1998).

[9] K. Yokoya, *Impedance of Slowly Tapered Structures*, Tech. Rep. CERN-SL-90-88-AP (CERN, 1990).

[10] G. Stupakov, Phys. Rev. ST Accel. Beams **10**, 094401 (2007).

[11] K. L. F. Bane, G. Stupakov, and I. Zagorodnov, Physical Review Special Topics - Accelerators and Beams **10**, 074401 (2007).

[12] G. Stupakov and B. Podobedov, Phys. Rev. ST Accel. Beams **13**, 104401 (2010).

[13] I. Zagorodnov and T. Weiland, Phys. Rev. ST Accel. Beams **8**, 042001 (2005).

[14] I. Zagorodnov, Phys. Rev. ST Accel. Beams **9**, 102002 (2006).

[15] W. Bruns, GdfidL: Electromagnetic field simulator, `https://www.gdfidl.de/`, accessed: 2026-09-27.

[16] A. E. Siegman, *Lasers* (University Science Books, Mill Valley, CA, 1986).

[17] M. Zhao, Y. Tao, K. Weber, T. Kaune, S. Schuster, Z. Hao, and G. Wanner, Sensors **23**, 9024 (2023).

[18] R. Paschotta, Fresnel number, RP Photonics Encyclopedia, available: https://www.rp-photonics.com/fresnel$_n$*umber.html*.

[19] X. E. Lin and D. H. Whittum, Phys. Rev. ST Accel. Beams **3**, 101001 (2000).

[20] V. E. Balakin and A. V. Novokhatski, in *Proceedings of the 12th International Conference on High-Energy Accelerators*, edited by F. T. Cole and R. Donaldson (Fermilab, Batavia, IL, 1983) p. 117.

[21] J. J. Bisognano, S. A. Heifets, and B. C. Yunn, in *Proceedings of the European Particle Accelerator Conference (EPAC 1988)* (Rome, Italy, 1988) pp. 708–710.

[22] S. A. Heifets and S. A. Kheifets, Rev. Mod. Phys. **63**, 631 (1991).

[23] F. W. J. Olver, D. W. Lozier, R. F. Boisvert, and C. W. Clark, eds., *NIST Handbook of Mathematical Functions* (Cambridge University Press, Cambridge, UK, 2010).

[24] DLMF, NIST Digital Library of Mathematical Functions, `https://dlmf.nist.gov/` (2026), release 1.2.8 of 2026-09-15; F. W. J. Olver, A. B. Olde Daalhuis, D. W. Lozier, B. I. Schneider, R. F. Boisvert, C. W. Clark, B. R. Miller, B. V. Saunders, H. S. Cohl, and M. A. McClain, eds.

[25] A. Blednykh and S. Krinsky, Physical Review Special Topics - Accelerators and Beams **15**, 054405 (2012).

[26] A. Blednykh and S. Krinsky, in *Proceedings of PAC2013* (Pasadena, CA, USA, 2013).

[27] G. Stupakov, in *Proceedings of PAC09* (Vancouver, B.C., Canada, 2009).

[28] P. L. Morton, *Introduction to Impedance for Short Relativistic Bunches*, Tech. Rep. SLAC-PUB-6052 (Stanford Linear Accelerator Center, 1993).

[29] A. Natochii, E.-C. Aschenauer, K. Hamdi, C. Hetzel, E. Llink, D. Marx, C. Montag, S. Tepikian, Y. Cai, and Y. Nosochkov, arXiv preprint (2025), arXiv:2512.19502.

[30] A. Natochii, E.-C. Aschenauer, J. Best, A. Blednykh, X. Gu, K. Gunavathi, C. Hetzel, and C. Montag, arXiv preprint 10.48550/arXiv.2610.04682 (2026), arXiv:2610.04682 [physics.acc-ph].